Three-dimensional upper crustal structure of the geothermal system in Tarutung (North Sumatra, Indonesia) revealed by seismic attenuation tomography

Umar Muksin,[1,2] Christian Haberland,[1] Klaus Bauer[1] and Michael Weber[1,3]

[1]*German Research Centre for Geosciences GFZ, Potsdam, Germany. E-mail: muksin@gfz-potsdam.de*
[2]*Department of Physics, Syiah Kuala University, Banda Aceh, Indonesia*
[3]*Institute of Earth and Environmental Science, University of Potsdam, Potsdam, Germany*

SUMMARY

The geothermal potential in Tarutung is controlled by both the Sumatra Fault system and young arc volcanism. In this study we use the spatial distribution of seismic attenuation, calculated from local earthquake recordings, to image the 3-D seismic attenuation of the area and relate it with the temperature anomalies and the fluid distribution of the subsurface. A temporary seismic network of 42 stations was deployed around Tarutung and Sarulla (south of Tarutung) for a period of 10 months starting in 2011 May. Within this period, the network recorded 2586 local events. A high-quality subset of 229 events recorded by at least 10 stations was used for the attenuation inversion (tomography). Path-average attenuation (t_p^*) was calculated by using a spectral inversion method. The spread function, the contour lines of the model resolution matrix and the recovery test results show that our 3-D attenuation model (Q_p) has good resolution around the Tarutung Basin and along the Sarulla graben. High attenuation (low Q_p) related to the geothermal system is found in the northeast of the Tarutung Basin suggesting fluid pathways from below the Sumatra Fault. The upper part of the studied geothermal system in the Tarutung district seems to be mainly controlled by the fault structure rather than by magmatic activities. In the southwest of the Tarutung Basin, the high attenuation zone is associated with the Martimbang volcano. In the Sarulla region, a low-Q_p anomaly is found along the graben within the vicinity of the Hopong caldera.

**Key words:** Seismicity and tectonics; Body waves; Seismic attenuation; Seismic tomography.

1 INTRODUCTION

The Tarutung region is one of the geothermal areas in Sumatra that the Indonesian government (the Center for Geological Resources) is planning to exploit. The geothermal potential in the region is manifested by several hot springs (represented by red stars in Fig. 1) along the Tarutung Basin. The most prominent geothermal manifestations are Sipoholon, Panabungan and Hutabarat (see large red stars in Fig. 1). As Tarutung is located on the Tarutung Basin along the Sumatra Fault and surrounded by young volcanoes and calderas, the whole tectonic system of the area is considered to play a significant role for the geothermal system (Muksin *et al.* 2013).

Geophysical methods were applied for a first evaluation of the geothermal potential around Tarutung including shallow seismics, geoelectrics and magnetotellurics (Niasari *et al.* 2012). Since Tarutung is located in a seismically active region along the Sumatra Fault, passive seismic methods can also be utilized. Previous seismological studies at a larger scale including the Tarutung area

were conducted at the near Toba caldera by using V_p and V_p/V_s tomography (Koulakov *et al.* 2009) and ambient noise tomography (Stankiewicz *et al.* 2010). However, these two studies were not resolving details of the Tarutung geothermal area. Therefore, a dense new passive seismological experiment was conducted in 2011 to achieve the resolution required for geothermal exploration around Tarutung (Muksin *et al.* 2013). The resulting V_p and V_p/V_s tomographic images revealed the geometry of the Tarutung and Sarulla basins as well as potential fluid pathways indicated by high V_p/V_s anomalies (Muksin *et al.* 2013).

In Tarutung, the existing V_p and V_p/V_s models (Muksin *et al.* 2013) can be complemented by studying seismic attenuation (Q^{-1}). In attenuation tomography, authors generally associate high intrinsic attenuation anomalies with high fluid flow, saturated rocks or cracks and/or high temperature or pressure zone (Evans & Zucca 1988; Zucca & Evans 1992; Zucca *et al.* 1994; Haberland & Rietbrock 2001; De Lorenzo *et al.* 2001). On the opposite, low-to-moderate attenuation is usually associated with dry and compact
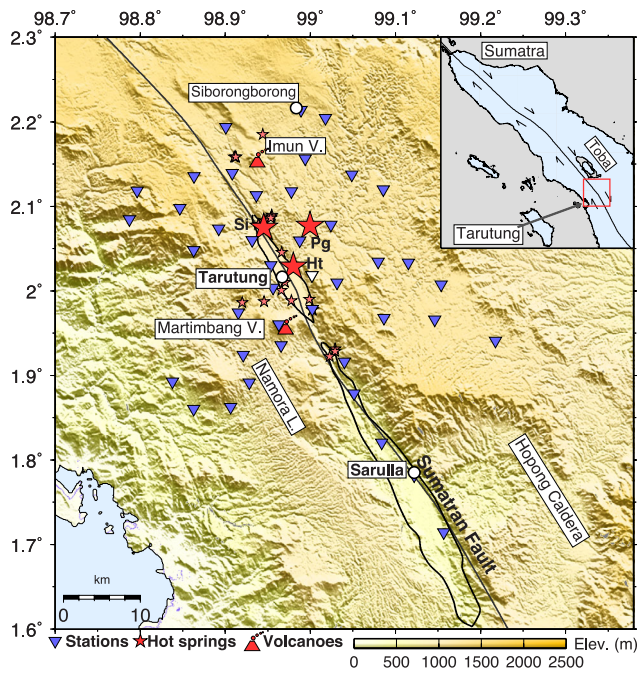
Figure 1. The seismic network deployed in Tarutung for 10 months. The Tarutung region is located just south of Lake Toba (inset map). Three main hot springs, represented by the large red stars, are located in Sipoholon (Si), Hutabarat (Ht) and Panabungan (Pg).

rocks. It has been proposed that attenuation is related to a variety of physical mechanisms rather than to chemical composition (e.g. Sato *et al.* 1989). Laboratory experiments have shown that seismic energy is dissipated through grain boundary interaction or intra-granular relaxation (Sato *et al.* 1989). The dissipation is different from one to another composition related with internal mechanisms. The presence of some amount of water in cracks or pores may attenuate seismic energy which lowers Q (Karato 2003). This mechanism is called viscous dissipation, which includes shear relaxation and pressure change within cracks or pores (Mavko *et al.* 1979; Walsh 1995). Another attenuation is caused by thermally activated mechanisms, which includes grain boundary relaxation and sliding (Sato *et al.* 1989). Melting or partial melting will dissipate seismic energy because of the pressure gradient within rocks and also lattices or atoms within materials are more mobile therefore seismic energy is easier to be absorbed. The sensitivity of intrinsic attenuation on temperature and fluid saturation (e.g. Zucca *et al.* 1994; Haberland & Rietbrock 2001; Martínez-Arévalo *et al.* 2005; De Siena *et al.* 2010) makes it an ideal parameter to study geothermal prospects. In addition, other processes such as geometrical spreading, multi-pathing and focusing/defocusing due to structural heterogeneities, reflection and transmission at structural boundaries, as well as scattering can cause redistribution of seismic energy, thus potentially contributing to the total or apparent attenuation (Q_t^{-1}).

In the Geysers geothermal field (United States), increased attenuation was found within the reservoir and the attenuation was higher at greater depth interpreted as fluid-saturated rocks (Zucca *et al.* 1994). High attenuation in the western central Andes correlates with the location of the magmatic arc and was associated with thermally weakened crust and partial melting (Haberland & Rietbrock 2001). Supported by the V_p and V_p/V_s tomography results and other geophysical data, attenuation tomography was able to distinguish gas and fluid reservoirs as well as hydrothermal basins in Campi Flegrei (De Siena *et al.* 2010). Priyono *et al.* (2011) revealed

high *P*- and *S*-wave attenuation anomalies beneath the Mt Guntur complex, West Java Indonesia, consistent with low *P* and *S* velocity. High attenuation was also found in a sediment basin and beneath the magmatic arc in central and east Java (Bohm *et al.* 2013).

The main aim of the study is to further constrain the nature of the geothermal system. The paper describes regional setting and experiment, data analysis and inversion for Q_p, and finally provides an integrated interpretation of Q_p together with the existing V_p and V_p/V_s models to improve the understanding of the geothermal system and its relation to the tectonic setting of the region. Several time-domain and frequency-domain methods have been developed to estimate attenuation of observed seismograms at various scales. The coda-Q (Q_c) estimation regularly used in crustal scale studies (e.g. Chung *et al.* 2009) utilizes the amplitude decay of the later parts of the seismogram as a function of time (and frequency; Aki & Chouet 1975). Q_c is often found to be frequency dependent, and considered to be related to scattering and intrinsic attenuation (e.g. Aki & Chouet 1975; Frankel & Wennerberg 1987). Alternatively, the analysis of spectra of certain phases (e.g. *P*, *PP*, *S*, *SS*; often body waves) is applied to global (e.g. Hwang *et al.* 2011), regional and local data. Spectral division is often used to remove some of the factors influencing seismic spectra (e.g. source effects, site effects) without knowing their exact form (e.g. Flanagan & Wiens 1990; Sanders 1993). Spectral inversion (including source parameters, site effects, attenuation) was successfully applied to data sets covering a broad range of scales, from the local scale (Scherbaum 1990; Boatwright *et al.* 1991; Rietbrock 2001) to the regional scale (Schurr *et al.* 2003). Pulse rise time (Gladwin & Stacey 1974), pulse widths (Wu & Lees 1996) and frequency shift (Quan & Harris 1997) methods are also utilized in the lab and on a local scale. In this paper we use a spectral inversion method to derive the path-averaged attenuation parameter t^* from body *P* waves and invert for the 3-D distribution of the quality factor Q_p using attenuation tomography.

2 REGIONAL SETTING

The variation of the geometry and morphology of the subduction zone beneath Indonesia reflects the changes in rate and direction of the Indo–Australian Plate motion. In Java, the Indo-Australian Plate motion is perpendicular to the trench correlating with the steep subduction zone. In Northern Sumatra, the plate motion becomes more oblique and even almost parallels the trench in Andaman, which could be related with the more gradual subduction zone (Pesicek *et al.* 2010). The oblique convergence between the Indo–Australian and Eurasian plates along Sumatra has produced the lateral-slip Sumatra Fault accommodating the trench-parallel component (Bellier & Sébrier 1994; Sieh & Natawidjaja 2000; McCaffrey 2009).

The 1900-km-long Sumatra Fault is segmented into 19 sections, locally represented by several pull-apart basins (Sieh & Natawidjaja 2000). The variation of the Indo–Australia plate motion is also related to the slip rate along the Sumatra Fault. Derived from stream offsets observed on SPOT images, the recent slip rate increases from less than 10 mm yr^{-1} in the Sunda strait at the southernmost to 11–19 mm yr^{-1} in central Sumatra, and 23 ± 2 mm yr^{-1} around Tarutung and Toba (Bellier & Sébrier 1995). Along the Sumatra Fault, the earthquakes are mostly strike-slip with the maximum magnitude of M_s 7.7 but some normal fault earthquakes occurred within the pull-apart basins (Sieh & Natawidjaja 2000). This normal faulting indicates simultaneous strike-slip motion and transform-normal extension within a strike-slip fault zone (Bellier & Sébrier 1994).

The Tarutung district covers the area of 98.7°E to 99.4°E and 1.6°N to 2.3°N centred around the diamond-shaped pull-apart basin with clearly defined borders. The Tarutung Basin is located between the two main features of the Sumatra Fault, the Toba caldera in the north and the bifurcation in the south. The Tarutung pull-apart basin is characterized by a presently active fault zone produced as a result of a larger step-over of the previous fault system in the Toba area and subsequent formation of the great Toba caldera within this older step-over region (Bellier & Sébrier 1994). To the south of Tarutung, there is an asymmetrical basin called Sarulla graben characterized by normal faults that parallel the weak major strike-slip fault (Hickman *et al.* 2004).

The volcanic arc, including the young volcanism along the Sumatra Fault, correlates with the geometry of the fault and the Sunda Trench (Sieh & Natawidjaja 2000). The Tarutung Basin is surrounded by the Martimbang, Helatoba (outside of the map) and Imun volcanoes as shown in Fig. 1. The yet undated Martimbang volcano is characterized as a young andesite basaltic cone (Hickman *et al.* 2004), while the Helatoba and Imun might have been created in Pleistocene (Gasparon 2005). Along the Sarulla graben, the volcanism includes the Hopong caldera, Namora-I-Langit dome field and Sibual-buali volcano (south of Sarulla), which are related to the weakening of the strike-slip fault. Along the Sumatra Fault, around 50 per cent of the geothermal manifestations are associated with pull-apart basins while the other half are related to volcanic activities (Muraoka *et al.* 2010). In the case of the Tarutung and Sarulla geothermal areas, both, the pull-apart basins and volcanic activities, might contribute to controlling of the geothermal system.

3 EXPERIMENT AND DATA

Fig. 1 shows our temporary network consisting of 42 short-period seismic instruments installed in the Tarutung and Sarulla region for 10 months starting 2011 May with an average station spacing of around 5 km. 40 stations were equipped with three-component short-period (1 Hz) sensors, and digital PR6-24 Earth Data Loggers sampling at 100 sps. Two additional stations were equipped with three-component 4.5 Hz geophones and DSS CUBE data logger (Omnirecs) recording data with 100 sps.

An automated picking procedure (Nippress *et al.* 2010) was used to identify the *P*- and *S*-wave arrivals from local events, which we then manually checked and revised. Our catalogue includes 2586 events recorded by at least eight stations. Waveforms with ambiguous onset were excluded. The HYPO71 routine (Lee & Valdes 1985) was then applied to determine the initial hypocentres. Eventually, 809 high-quality events with gap angles smaller than 180° were relocated by using 1- and 3-D inversion for velocity structure and hypocentre relocation. Details of this data analysis as well as the resulting seismicity distributions and V_p and V_p/V_s structure can be found in Muksin *et al.* (2013). Among these 809 events, only 229 events with high-quality waveforms are used in the seismic attenuation tomography (discussed in the next section).

4 METHODS

4.1 Formulation of seismic attenuation

The amplitude spectrum $A_{ij}(f)$ of body/*P* wave of a source *j* observed at receiver *i* can be expressed in the following way (Scherbaum 1990; Sanders 1993):

$$A_{ij}(f) = S_j(f) \cdot R_i \cdot (f) I_i(f) \cdot B_{ij}(f) \cdot G_{ij}, \tag{1}$$

where *f* is frequency, $R_i(f)$ is the receiver site effect, $I_i(f)$ is the instrument response and G_{ij} is the geometrical spreading, which we assume to be frequency independent. The source spectrum $S_j(f)$ can be described following, for example, Scherbaum (1990) as:

$$S_j(f) = \frac{\Omega_{oj}}{1 + \left(f^\gamma/f_{cj}^\gamma\right)}, \tag{2}$$

where Ω_o represents the long-period spectral level, γ is the high-frequency decay rate and f_{cj} is the corner frequency. Eq. (2) is equivalent to a Brune-type ω^2 source model (Brune 1970, 1971; Hanks & Wyss 1972) when $\gamma = 2$. The attenuation spectrum of seismic *P* waves is defined as (Sanders 1993)

$$B_{i,j}(f) = \exp(-\pi t_{ij}^* f). \tag{3}$$

The path-averaged attenuation t^* is determined from the rock properties along the ray path, in particular from the (specific) attenuation $Q_p^{-1}(r)$ and the seismic *P*-wave velocity $V_p(r)$ (see e.g. Scherbaum 1990) as

$$t_{ij}^* = \int_{ray} Q_p^{-1}(r) v^{-1}(r) \, dr + \tau_i^*. \tag{4}$$

The parameter τ_i^* is a constant accounting for the attenuation beneath the station (so-called station correction). Assuming Q_p to be frequency independent, the amplitude spectra from the combination of eqs (1)–(3) can be expressed by

$$A_{ij}(f) = \frac{\Omega_{oj}' \exp(-\pi t_{ij}^* f)}{1 + \left(\frac{f^2}{f_{cj}^2}\right)}, \tag{5}$$

where Ω_{oj}' is the signal moment taking up the source moment Ω_{oj} and all frequency-independent factors possibly influencing the spectrum between the source and the receiver (e.g. Haberland & Rietbrock 2001).

To estimate the above-mentioned attenuation parameters, a 2.56-s time window centred at the *P*-wave arrivals was analysed using a multitaper technique (Park *et al.* 1987). We also analysed the time window before the *P*-wave arrival to assess the signal-to-noise ratio (Fig. 2). In the inversion we simultaneously calculate the following free parameters: (1) individual seismic attenuation along the propagation path t_{ij}^* for each observation of an event, (2) individual signal moment Ω_{oj}' and (3) a single source corner frequency f_{cj} for all records of an event using a non-linear spectral inversion method (e.g. Rietbrock 2001; Eberhart-Phillips & Chadwick 2002). It is well known that the source corner frequency f_c and the t^* values have a quite similar effect on the shape of earthquake spectra yielding ambiguities when inverting single spectra (e.g. Scherbaum 1990; Boatwright *et al.* 1991). The approach of inverting for individual seismic attenuation parameters t_{ij}^* and a single source corner frequency f_{cj} common for all observations of an event proved to reliably separate these factors when a sufficiently large number of spectra are used (Rietbrock 2001; Haberland & Rietbrock 2001; Eberhart-Phillips & Chadwick 2002; Bohm *et al.* 2013).

In this inversion a frequency band between 1 (at the lower boundary) and 10–30 Hz (at the upper boundary), depending on noise, was analysed. Only events having at least 10 usable observations were included (i.e. with a signal-to-noise ratio higher than 1.4) resulting in a final data set of 3968 t^* values of 229 events, which were used in the tomographic inversion. The misfit between observed and synthetic spectrum is used as weight *w* in the tomographic inversion for Q_p. Fig. 2 shows four examples of the spectral analysis of an event located in the Tarutung Basin and Fig. 3 shows the Q_p values
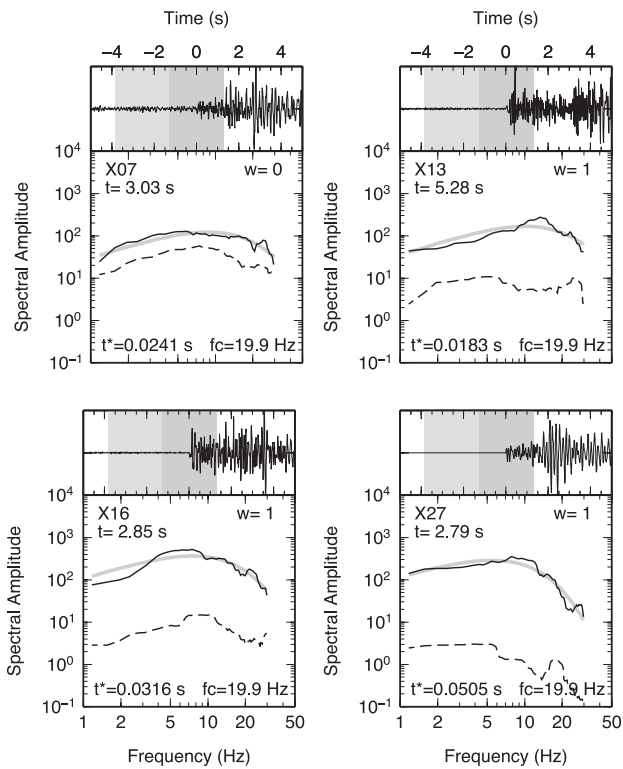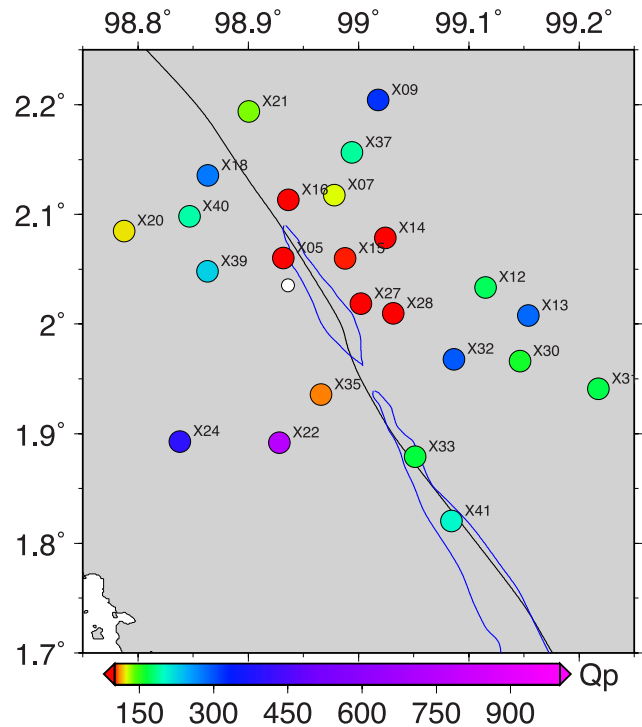
Figure 2. The calculation of t^* values using spectral analysis of four records (stations X07, X13, X16, X27) of an event (the location is shown in Fig. 3) occurred on 2013 November 20. t is traveltime, w is the weight representing the quality of the waveforms and f_c is the source corner frequency. The top panels show the normalized time-series. The signal is within the darker shading windows following the noise in the lighter shading windows. The bottom panels show the noise spectrum (dashed lines), signal spectrum (black lines) and estimated spectrum resulting from spectral inversion (light-bold lines).

Figure 3. Estimated Q_p values of all observing stations of an event marked by the white circle. The corresponding t and t^* values are shown in Fig. 2 for four stations showing low Q_p values for station closed to the basin, located in the northeast of Tarutung.

recorded by each station (Fig. 4 gives the location of the 229 events used).

The uncertainty of the data is derived from the assessment of t^* of similar source–receiver ray paths for which we expect similar values. We divided the region into $500 \times 500 \times 250$ m cells and analysed all t^* values originating from an identical cell and recorded by the same station. We considered the cell containing at least two events recorded by the same station and finally we obtained and analysed 436 data points. Fig. 5(a) shows the t^* values having consistent deviation values relative to their averages. The standard deviation of the t^* data of similar ray paths is found to be 0.006 s as shown in Fig. 5(b). We assume that this value is representative for the uncertainty of our t^* data set. Some previous studies found a variation of data uncertainty depending on the t^* values [i.e. Haberland & Rietbrock (2001) observed higher uncertainties for larger t^* values], however our data show a relatively constant data uncertainty. Very similar t^* values of almost the same ray paths (from different, however, closely located earthquakes having different source characteristic) corroborate the assertion that our spectral inversion method can indeed successfully separate between path and source effects.

4.2 Attenuation tomography

Having determined the t^* values of all source–receiver configurations, the 3-D absorption structure Q_p^{-1} was derived by using the

SIMUL2000 tomographic inversion code (Thurber 1983; Eberhart-Phillips & Michael 1998; Rietbrock 2001). The 3-D model grid was centred at 99.0°E and 2.0°N and was oriented following the trend of the major structures within the study area. The node spacing was chosen as 3×3 km laterally (Fig. 4) and 2 km vertically in the central part of the model. Outside this area or deeper than 16 km (the maximum of the events depth), the grid nodes are spaced coarser. We use the same grid spacing as in the traveltime tomography (V_p, V_p/V_s; Muksin *et al.* 2013). Considering an average station distance of around 5 km we choose a lateral node spacing of 3 km. Vertical node spacing is chosen smaller since the velocity structure is layered vertically (Kissling *et al.* 1994) and seismicity is distributed in a narrow depth range (between 6 and 16 km). Muksin *et al.* (2013) demonstrated that with this chosen node spacing the consistent and stable V_p and V_p/V_s velocity models were achieved with very low rms values.

The Q_p inversion was started from a homogeneous model with a constant Q_p of 165. This value is the average of all the path-averaged quality factors $Q_p(r)$ for all source and receiver pairs. The P-velocity model was taken from the 3-D traveltime tomography of Muksin *et al.* (2013). P velocity, hypocentre coordinates and origin times were not modified during the Q_p inversion. The trade-off curve between the variance of data misfit and the model variance was used to determine the damping factor for the inversion (Eberhart-Phillips 1986).
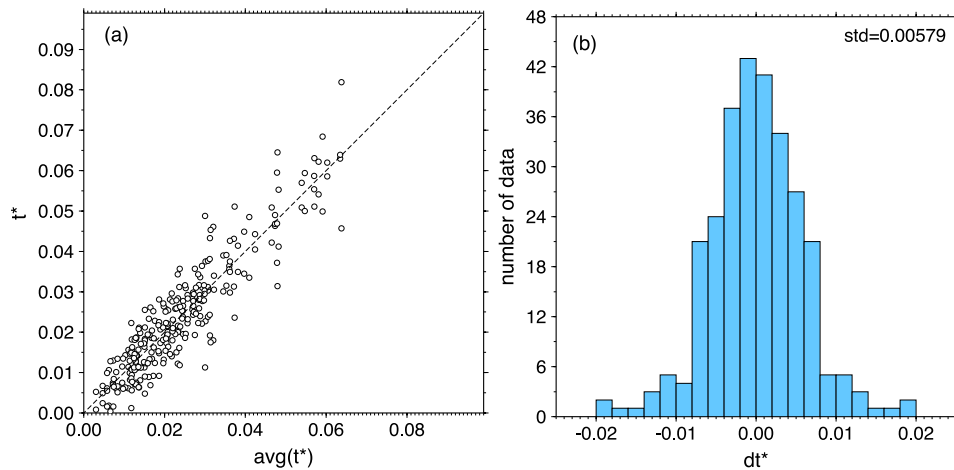
4.3 Assumptions and limitations

Our method is based on a number of assumptions, which are summarized here.

Often, a frequency-dependent Q_p is assumed (often a power-law formulation, $Q(f) = Q_0 f^\alpha$, with $0 < \alpha < 1.0$), from laboratory
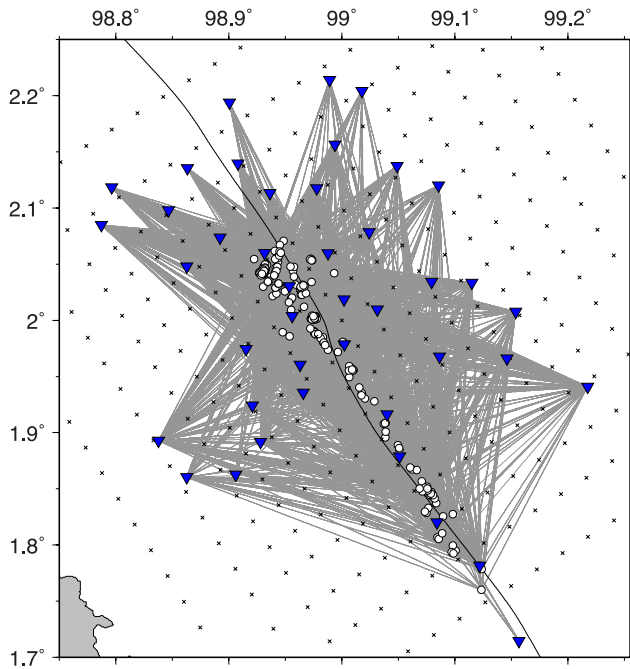
Figure 4. The design of the 3 × 3 km grid node spacing rotated parallel the Sumatra Fault. The grey lines represent the ray paths propagate from events (white circles) to stations (blue triangles). The small cross marks represent the nodes.

studies (e.g. Faul *et al.* 2004) to regional (Atkinson 2004) and global studies (e.g. Anderson & Given 1982). We have checked this assumption in our data and ran different inversions for different values of α. The best overall spectral fit was achieved with $\alpha = 0.0$, however, moderate values of α between 0.0 and 0.2 gave similar good spectral fits. This finding confirms results from other studies which also found best fits for frequency-independent Q (Rietbrock 2001; Bohm *et al.* 2013). However, frequency-independent Q would be higher, and this should be considered when comparing results to different studies (see e.g. Eberhart-Phillips & Chadwick 2002). Nevertheless, we interpret mainly the relative attenuation anomalies (shape, location and size) and not the absolute Q values, so this issue is not affecting our conclusions.
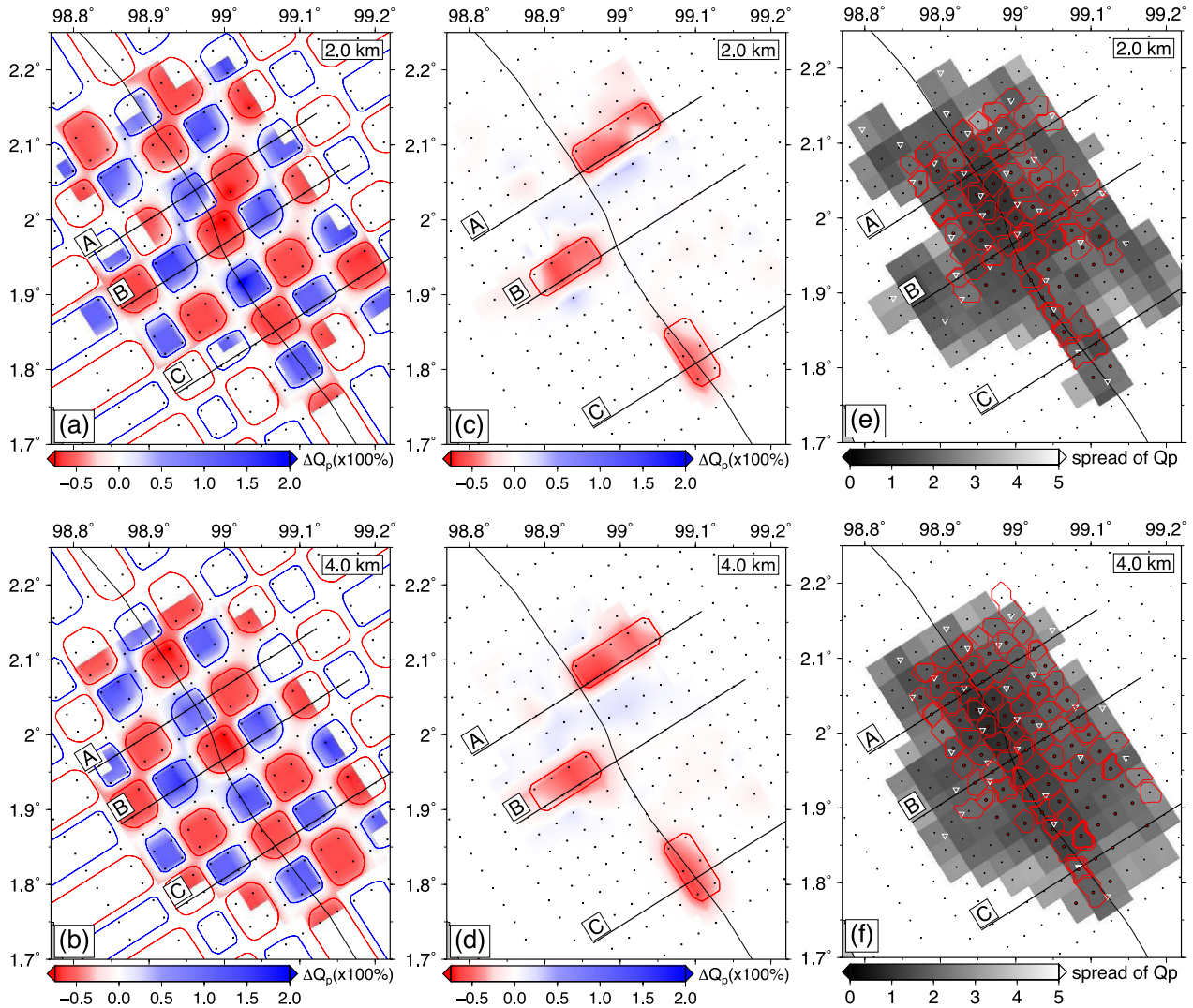
We assume that both intrinsic and scattering attenuation contribute to the total (or apparent) measured attenuation. In the interpretation we assume that Q_p is dominated by intrinsic attenuation and not by scattering; however, we have not quantified it yet (topic for future study). Nevertheless, we think that intrinsic attenuation is more prominent in our data since we do not observe long coda indicating strong scattering effects in our records and we analyse the early part of the seismogram mainly including direct wave energy.

We assume a frequency-independent geometrical spreading. Due to the spherical divergence the amplitude of body waves in a homogeneous medium decrease with $1/r$. Realistic velocity models are known to produce a more complex amplitude behaviour, and head waves, surface waves and guided waves even show frequency-dependent geometrical spreading (e.g. Yang *et al.* 2007; Morozov 2010). In our data set we only expect body P waves (*Pg* up to ~40 km) for which we expect a $1/r$ geometrical spreading, not *Pn, Sn, Sg, Lg*, surface waves, etc. We calculate the attenuation from the spectral decay—frequency-independent geometrical spreading would not bias our t^* estimates.

We assume an ω^2 source model (e.g. Aki 1967; Aki & Richards 1980). For a data set from Japan and using a similar analysis technique Rietbrock (2001) found that the ω^2 model gave significantly better spectral fit than the ω^3 model. We expect a similar behaviour in our data set.

5 RESOLUTION AND RECOVERY TESTS

The quality of our tomographic model is examined by evaluating the model resolution matrix and the spread function (Toomey & Foulger 1989). The spread values (represented by the grey colour scale in Figs 6e and f and 7g–i) describe how well a model node parameter is resolved and how other nodes at some distance influence the resolution of a particular node. To assess the smearing of each node, we visualize the contour lines of the model resolution [represented by red contour lines in Figs 6e and f and 7g–i for each node (Eberhart-Phillips & Michael 1998)]. The model nodes with small spread function values and localized contour lines are considered to be well resolved. The quality of the inversion results is also investigated by using two different recovery tests: checkerboard tests and synthetic tests with characteristic models.

Figure 5. For estimating the uncertainty of the derived t^* values, we compared the t^* values of similar ray paths, that is, from collocated earthquakes (within 500 × 500 × 200 m blocks) observed at a particular station. (a) Comparison between t^* values and the average of t^* of each cell. (b) The standard deviation is 0.006 s, which we assume to be the average uncertainty of the t^* values.

Figure 6. The checkerboard, characteristic models, spread function and resolution matrix at depth of 2 and 4 km used to analyse the quality of the results: (a) and (b) show the checkerboard recovery results, the blue (red) boxes indicate the high (low) Q_p values; (c) and (d) represent the characteristic feature recovery tests; (e) and (f) show the spread values (represented by the grey colour bar) and the contour lines of model resolution matrix (red contour lines) in map view.
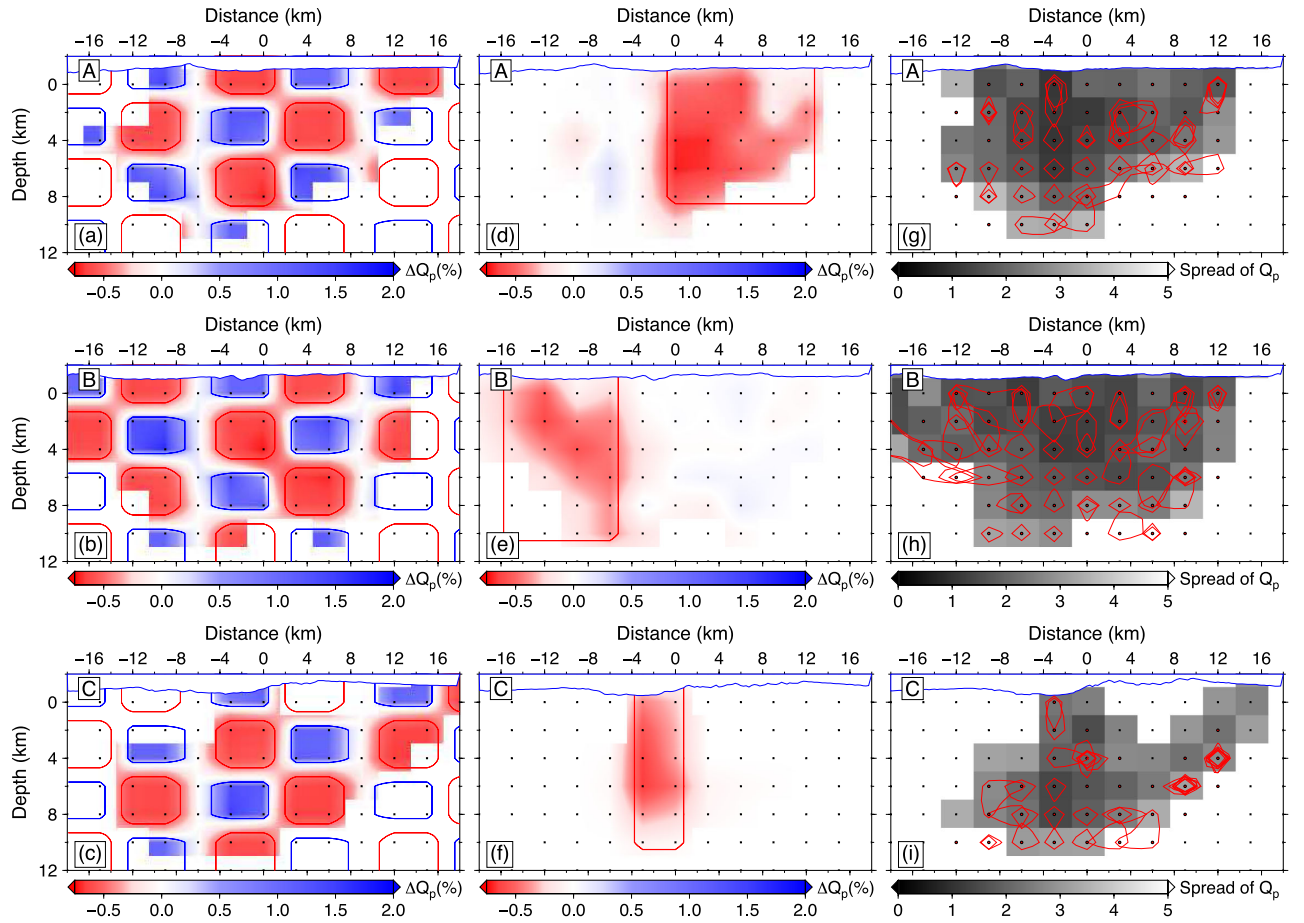
The checkerboard recovery tests complement the resolution matrix analysis providing the information of how the inversion could resolve arbitrary given anomalies. For the checkerboard tests the background model $Q_p = 165$ (according to the background model for the real inversion) is perturbed by -100 and $+250$, respectively, for the low and high Q_p anomalies. Each anomaly covers four grid nodes laterally and two in vertical direction as shown in Figs 6(a) and (b). The high and low Q_p imposed anomalies are indicated by red and blue colours, respectively.

The characteristic synthetic model was constructed based on the results of the real inversion and the tectonic setting of the area to investigate the resolution of the expected anomalies. In the characteristic models we imposed high attenuation anomalies (low Q_p) along the basins, around the Martimbang young volcano (southwest of Tarutung) and in the northeast of Tarutung where the major fluid discharges are situated. The low Q_p for the characteristic synthetic model is derived by perturbing the background model $Q_p = 165$ by -100. The characteristic synthetic model is represented by the red shapes in Figs 6(c) and (d). To simulate realistic conditions in

these recovery tests, we added Gaussian noise with a standard deviation of 0.0058 s to the synthetic t^* data for both, the checkerboard and characteristic models, based on the uncertainty estimations described in Section 4.2.

Some smearing in the checkerboard tests is produced among blocks containing similar anomalies represented by the presence of the shaded anomalies with small amplitude. The analysis of smearing is complemented by the analysis of the resolution matrix designated by the red contour lines in Figs 6(e) and (f). The checkerboard test results show that the high and low attenuation anomalies could be resolved and the images are not influenced by the distribution of the events. The application of the error (Gaussian noise) does not significantly alter the inversion results of the synthetic tests which means that the error of the data is still in a tolerable range.

Small spread function values (represented by the grey colour bar in Figs 6e and f) with the 70 per cent smearing contour line at different depth indicate well-resolved nodes with relatively less horizontal smearing in the vicinity of the Tarutung Basin (in the north) where the major geothermal manifestations are located. In

Figure 7. (a)–(c) Checkerboard recovery results along the cross-sections A–C indicated in Figs 6(a) and (b). (d)–(f) The characteristic feature recovery tests along the cross-sections A–C drawn in Figs 6(c) and (d). (g)–(i) The spread values (represented by the grey colour bar) and the contour lines of model resolution matrix (red contour lines) in vertical view along the cross-section A–C indicated in Figs 6(e) and (f).

accordance with the spread function, both, the checkerboard and the characteristic models are resolved and better recovered at deeper regions. These synthetic tests show that similar high attenuation anomalies located in the northern part around Tarutung could be imaged in the inversion of the real data. To the south, along the Sarulla graben, the nodes are well resolved only along the Sumatra Fault as the stations could only be located along the accessible roads close to the Sumatra Fault. The nodes outside the fault line are influenced by the nodes along the fault line as indicated by smearing contours of the model resolution matrix. Therefore, the only anomalies resolved are the ones along the main fault or in the vicinity of the Sarulla graben as demonstrated by the recovery tests (Figs 6a and b).

Fig. 7 shows the vertical view of the spread function values (represented by grey colour scale) and the smearing contour lines (red contour lines), as well as the recovery test results along the lines indicated in Fig. 6, which indicates a good resolution of our inversion results around the Tarutung Basin (in the north of Tarutung district). The nodes out to 8 km to the right and the left from the Sumatra Fault line are resolved, but experience smearing effects by their neighbours. Vertically, both the checkerboard and the characteristic anomalies are well resolved around the Tarutung Basin and only anomalies close to the fault are recovered in Sarulla.

The comparison of the distribution of the spread function with the region with good recovery of the synthetic structures indicates that model regions with a spread value of 2.5 and below are well

resolved. Accordingly, we show only these model regions in Figs 6 and 7.

6 RESULTS AND DISCUSSION

Fig. 8 (left panels) shows the map view of the attenuation structure of the region at different depth levels while Fig. 9 (left panels) displays the vertical images of the structure along the cross-sections (A–D marked in Fig. 8). In order to enrich the discussion, we complement Fig. 8 with the map view of the V_p (Fig. 8, middle panels) and V_p/V_s structure (Fig. 8, right panels). We also include the vertical view along the four cross-sections of the V_p (Fig. 9, middle panels) and the V_p/V_s structure (Fig. 9, right panels) obtained from Muksin *et al.* (2013). The results of the analysis of the data and the model quality from the spread function and the recovery tests confirmed the good resolution of the 3-D Q_p structure of the Tarutung geothermal area. Accordingly, we only show the structure located in the areas containing well-resolved nodes based on small spread function values. We have experimented applying different damping parameter for station correction used in damped least-square inversion to investigate the ambiguity of the tomography results. The higher damping parameter we apply, the lower station correction we observe. With different damping parameter, even with an extreme damping parameter (zero station correction), the shape of the anomalies is relatively stable but the amplitude of the anomalies
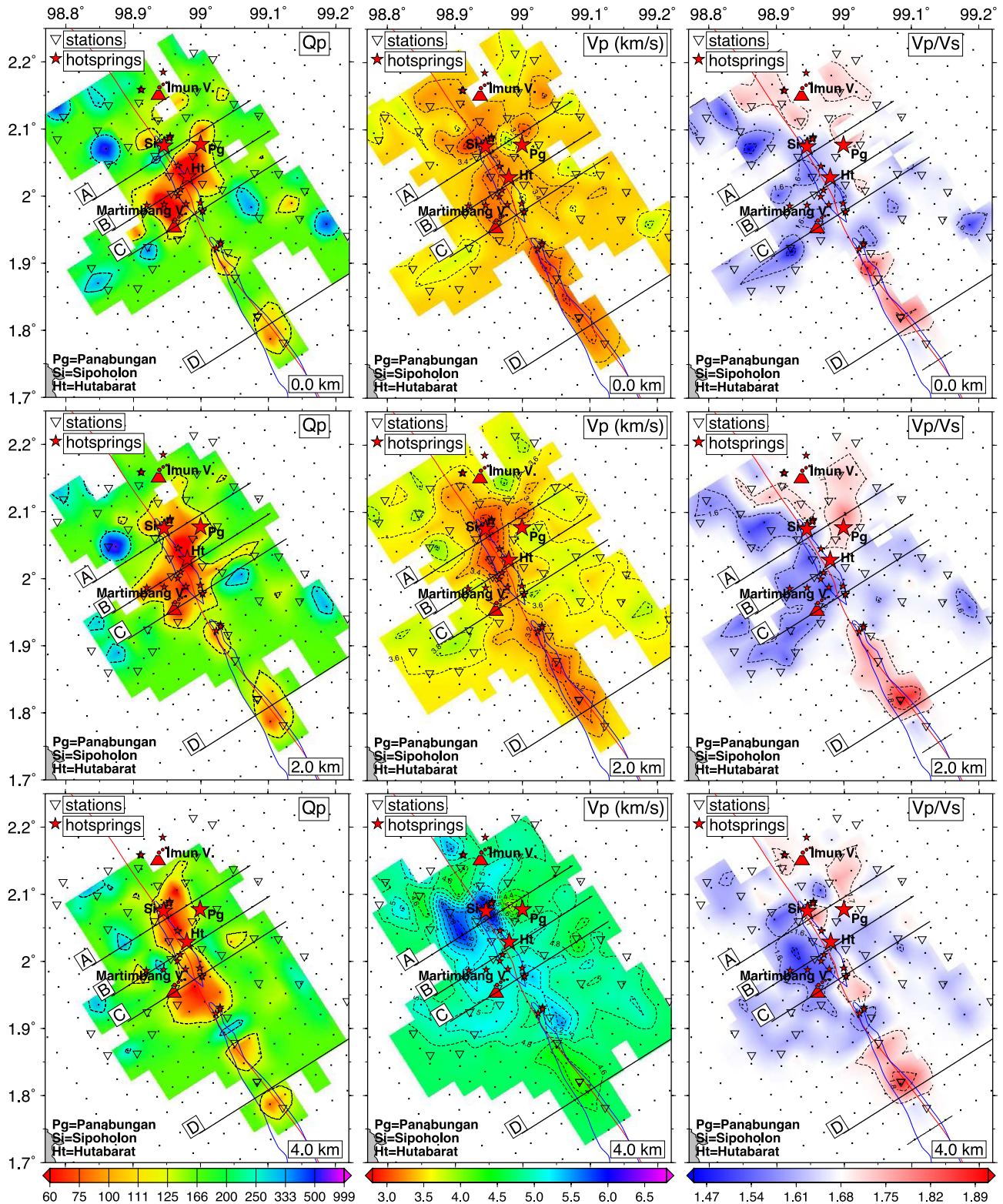
Figure 8. The map view of the attenuation structure (left panels), the V_p structure (middle panels) and the V_p/V_s structure (right panels) at depths of 0, 2 and 4 km. The structure along the profile A–D are shown in Fig. 9. The blue contour lines along the fault symbolize the Tarutung Basin (in the north) and Sarulla graben (in the south). The V_p and V_p/V_s structure are obtained from Muksin *et al.* (2013).
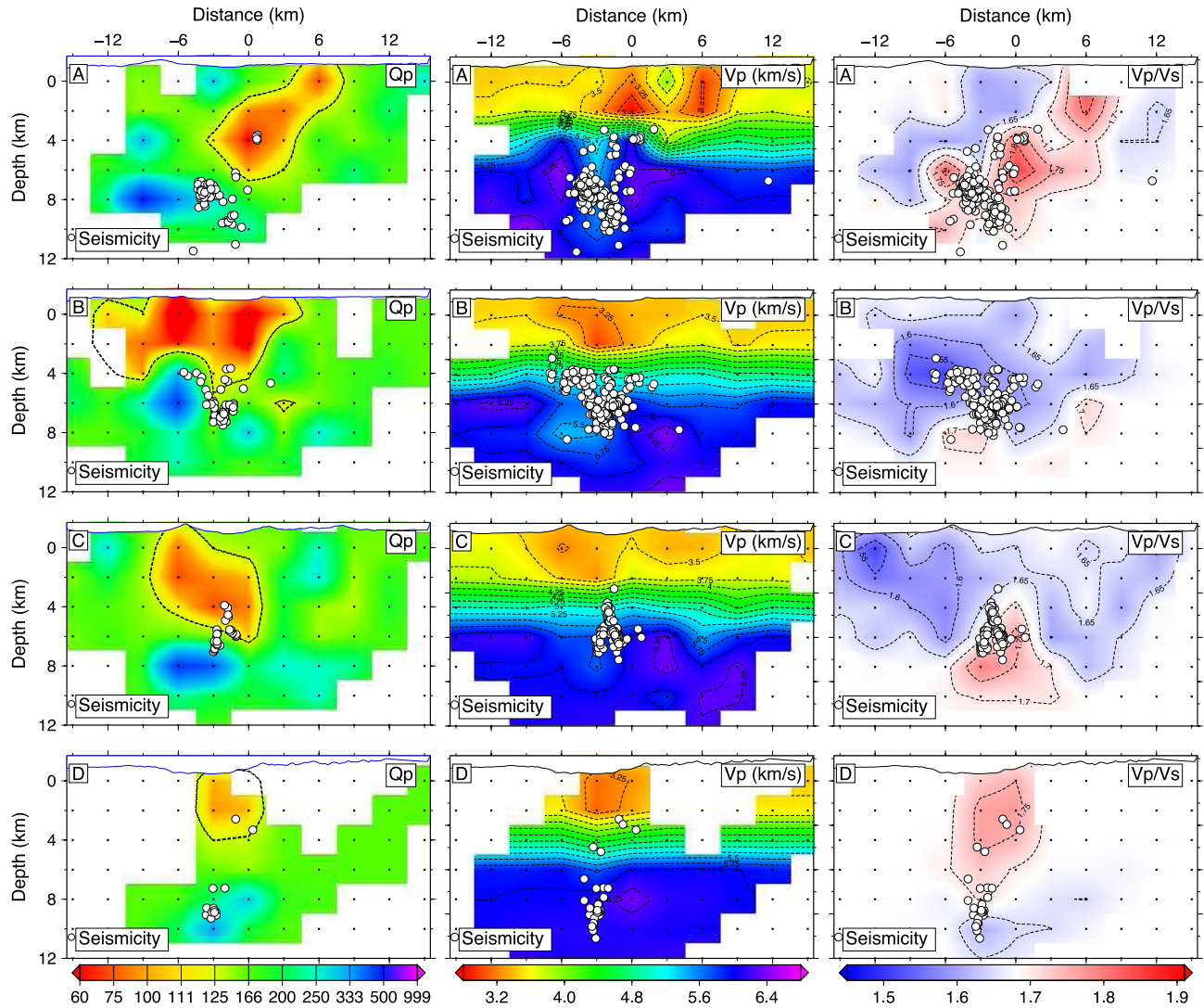
Figure 9. The vertical cross-section along the four profiles (A–D indicated in Fig. 8) of: the Q_p structure (left panels), the V_p structure (middle panels) and the V_p/V_s structure (right panels). The V_p and V_p/V_s structures are obtained from Muksin *et al.* (2013).

becomes more prominent and larger. Here, we use the damping parameter for station correction, which produces the station correction in the average of ∼0.003 s, which is smaller than the data uncertainty 0.006 s.

In general the low Q_p anomalies (high attenuation zones) are in a good agreement with the low V_p anomalies. We observe four different groups of high attenuation zones (Fig. 8) with $Q_p < 100$: (1) along the Tarutung Basin at depth shallower than ∼2 km; (2) in the northeast of the Tarutung Basin where the three major and high temperature geothermal manifestations (Sipoholon, Hutabarat and Panabungan) are located; (3) within the vicinity of the Martimbang young volcano, just southwest of Tarutung Basin, along the cross-section B in Fig. 8 and (4) along the Sarulla graben especially within the area of the Hopong caldera (see also Fig. 1).

From the description, seismic attenuation seems to be mainly controlled by physical properties such as temperature, pressure and porosity (Mavko 1980; Sato *et al.* 1989). Hence, the attenuation tomography results complement the velocity models and contribute to a consistent interpretation. The material properties related to the

attenuation and seismic velocity derived from laboratory works and tomography results are presented in Table 1.

6.1 Tarutung Basin and northeast of Tarutung

The attenuation result shows high attenuation along the Tarutung Basin with Q_p lower than 100 at shallow depth (<2 km; Fig. 8, left panels and Fig. 9, left panels). This low Q_p correlates with the low velocity (Muksin *et al.* 2013; Fig. 8, middle panels and Fig. 9, middle panels) and high electrical conductivity measured by the magnetotellurics (Niasari *et al.* 2012). Low Q_p zones related to the sedimentary basin are also found in other areas as briefly described in Table 1. Bohm *et al.* (2013), for example, found high attenuation ($Q_p < 100$) in Kendeng Basin south of the modern volcanic arc in Central Java. At shallow depths Hauksson & Shearer (2006) found low Q_p (≤100) along the Ventura and Los Angeles Basin in southern California, United States. We suggest that the low Q_p along the Tarutung Basin is related to unconsolidated material and high porosity of the sedimentary deposit mostly filled by the Toba

Table 1. Summary of material properties related to attenuation and seismic velocity based on laboratory experiments (lab) and field experiments (field).

Characteristic of Q, V_p, V_p/V_s and other geophysical properties	Lab/Field	Reference
Q_p decreases rapidly with increasing temperature	Lab	Sato *et al.* (1989)
Low Q_p correlated with the increased on the melting volume correlating and high temperature	Lab	Mavko (1980)
Q_p decreases with the increase of fluid content	Field	Haberland & Rietbrock (2001)
Sedimentary basin and magmatic in Central Java ($Q_p < 100$; low V_p; high electrical conductivity)	Field	Bohm *et al.* (2013)
Ventura Basin California (low $Q_p < 100$)	Field	Hauksson & Shearer (2006)
Low V_p and high V_p/V_s is related to high fluid saturation	Field	Julian *et al.* (1996) Husen *et al.* (2004) Haberland *et al.* (2009)
Low Q, low V_p and low V_s beneath Mt Guntur complex	Field	Priyono *et al.* (2011)
Gas filled volume beneath the Yellowstone caldera (low V_p and low V_p/V_s)	Field	Husen *et al.* (2004)
Change from liquid to vapour-rich state after extensive exploitation in the Geyser geothermal field (low V_p and low V_p/V_s)	Field	Julian *et al.* (1996)
CO_2 emission beneath the Mammoth Mountain in the Long Valley caldera (low V_p and low V_p/V_s)	Field	Julian *et al.* (1998)

tuff 74 000 yr ago from the great Toba eruption (Hickman *et al.* 2004).

The lowest Q_p values ($\sim$40) are observed in the area of the geothermal manifestation in the northeast of Tarutung. Usually, within the volcanic and geothermal areas, significantly low Q_p values are observed. Wu & Lees (1996), for example, observed an average of Q values of $\sim$30 within the area of Coso hot springs, California, United States. High attenuation in the northeast of Tarutung (Fig. 8, left panels and profile A in Fig. 9, left panels) is in good agreement with a high V_p/V_s zone (Fig. 8, right panels and profile A in Fig. 9) and is also consistent with a high electrical conductivity anomaly obtained from a preliminary modelling of magnetotelluric data (Niasari *et al.* 2012). We suggest that this region of high attenuation, low V_p, high V_p/V_s and high electrical conductivity is related to high fluid content. This conclusion is supported by the fact that the anomaly is surrounded by the three prominent geothermal manifestations. These three major manifestations have different physical characteristics. In Panabungan and Hutabarat, the hot springs have a similar temperature of 50 and 53 °C, respectively, high fluid flow rate and are localized in small areas. On the other hand, in Sipoholon, the temperature of the hot spring is higher (60 °C) and several small hot springs with less flow rate are distributed within a wider area and also characterized by the presence of travertine.

Although these three major manifestations have different temperature and apparent characteristic, they seem to originate from the same source from below the fault as shown in profile A of Q_p structure in Fig. 9 (left panels), as also confirmed by the V_p/V_s tomography (profile A of the V_p/V_s structure of Fig. 9, right panels). We suggest that hot fluids from the same source are moving along different pathways to the surface resulting in the variations of the physical characteristics of the geothermal manifestations (such as temperature and rock porosity). The reason of the northeastern trend of the fluid flow remains unsolved. To the east the rocks might be more permeable as also indicated by low resistivity (Niasari *et al.* 2012). Alternatively (or in addition), to the northeast of the Tarutung Basin several normal faults are found (indicating dilatation in this region), which could act as pathways for the fluid. From this analysis and our interpretation we conclude that the shallow geothermal system in the northeast of Tarutung is more controlled by the fault structure rather than by volcanism.

However, the high V_p/V_s anomaly is located more to the east, while the low Q_p zone is located closer to the basin. We suggest that V_p/V_s is more sensitive to high fluid content and images the higher

flow rate geothermal potential represented by Panabungan manifestation. The Q_p, on the other hand images the higher temperature geothermal potentials represented by the manifestation Sipoholon and Hutabarat and also the higher flow rate geothermal potential (Panabungan).

6.2 Martimbang volcano

Just to the southwest of Tarutung Basin, high attenuation is found in the vicinity of the Martimbang volcano (Fig. 8, left panels). At 2–3 km depth, the area of high attenuation (low Q_p) is located just below the volcano. However, Muksin *et al.* (2013) could not find a high V_p/V_s anomaly (V_p/V_s structure in Fig. 8, right panels) below the Martimbang volcano. Both Q_p and V_p/V_s are influenced by the physical properties such as pressure, temperature and pore fluids. According to laboratory results (Sato *et al.* 1989) and tomography results (e.g. Artemieva *et al.* 2004), attenuation significantly depends on temperature of rocks. On the other hand, compared with attenuation, V_p/V_s values depend less significantly on temperature changes (Wang & Nur 1990) and the effect might be too small to be observed in the tomography anomaly (Husen *et al.* 2004).

Several authors (e.g. Priyono *et al.* 2011) suggested that low Q_p, V_p and V_s beneath volcanoes are related to magmatic system. Others associate the low V_p/Vs anomalies within geothermal or volcanic areas with an increase of gas content. Husen *et al.* (2004), for example, interpreted a low V_p and low V_p/V_s zone as a gas-filled volume beneath the Yellowstone volcanic field. Julian *et al.* (1996) observed a significant decrease in V_p/V_s in the most exploited reservoir in the Geyser geothermal production field because of the change from liquid to vapour-rich state after extensive exploitation. Julian *et al.* (1998) found a low V_p/V_s anomaly related to the CO_2 emission beneath the Mammoth Mountain on the southwestern rim of Long Valley caldera, California, United States. The decrease in V_p/V_s due to the gas content pore fluid is caused by the very low bulk modulus of gas compared with that of liquids. Takanami *et al.* (2000) suggested that low Q and low seismic velocity beneath the Sawauchi volcanic front in northeastern Japan is related to a high-temperature zone without partial melting (very locally partial melting). However, in the area of the Martimbang volcano, there is no gas or vapour manifestation observed. In conclusion, we suggest that the low Q_p in the region without V_p/V_s anomaly (normal V_p/V_s) below the

Table 2. Low Q_p zone associated with the characteristic of the structure.

Areas	Characteristic	Interpretation
Along the basin	Low Q_p (<100) and low V_p	Sedimentary deposit
Southwest of the basin	Low Q_p (<100), normal V_p and V_p/V_s	Martimbang volcano
Northeast of the basin	Low Q_p (<100), low V_p and relatively low V_p/V_s	Hot fluid related area coincides with the location of the large hot springs
South of Tarutung (along the Sarulla graben)	Low Q_p (<100), low V_p, low V_s and high V_p/V_s	Hopong caldera and weak fault zone

Martimbang volcano is associated with high-temperature structure with a small amount of fluid or high temperature without or with a small amount of partial melting. At 4 km depth (Q_p structure in Fig. 8), the high attenuation anomaly is located close to the Sumatra Fault. This high attenuation could be interpreted as the pathway of the magma and/or hot fluid/gas of the Martimbang volcano fed from below the fault and transported to the left (southwest) of the fault as described in profile C in Fig. 9, left panels.

6.3 Sarulla region

The limited resolution of the inversion only allows us to image the structure in Sarulla region just below the Sumatra Fault. We found low Q_p anomaly along the basin, consistent with low V_p, low V_s and high V_p/V_s (Muksin *et al.* 2013). The low V_p and high V_p/V_s along the Sarulla graben is associated with a weak fault zone, caused by the volcanism, where numerous earthquakes occur along the graben. The high V_p/V_s could be also influenced by the high pressure of high-temperature fluid flow in the area as revealed by drilling results (Hickman *et al.* 2004). However, the low Q_p zone is located more to the south within the vicinity of the Hopong caldera (see Fig. 1 for the topography comparison). Therefore, we interpret low Q_p as being caused mainly by the presence of hot magma below the caldera and also by graben sediment. The heat source is still fed to the caldera along the fault system from below directly to the surface (profile D of Q_p and V_p/V_s structure in Fig. 9). Therefore, the presence of the Hopong caldera could significantly contribute to the control of the geothermal system in this area.

6.4 Conceptual structure of the Tarutung region

From the results and the discussion we can summarize the features of the attenuation properties derived from the attenuation tomography and complemented by the V_p and V_p/V_s tomography as shown in Table 2 and in the conceptual model in Fig 10. The layering in the model is derived from the V_p structure while characteristics of the geothermal system are derived from the V_p/V_s and the Q_p structure.

The Tarutung area consists of three main clusters (Fig. 10a): the Tarutung Basin, the magmatic system (southwest of Tarutung Basin) and the geothermal resource (northeast of the Tarutung Basin). The shape of the Tarutung Basin (light blue Fig. 10a) obtained from the V_p model (Muksin *et al.* 2013) correlates well with the geometry of the basin derived from the topography with depth of around 2 km (Fig. 8, middle panels). The geothermal potential manifested by the three big hot springs (Sipoholon, Hutabarat and Panabungan) in the eastern Tarutung is imaged by the red zone. The hot fluid for all geothermal potentials is fed from below the fault (Fig. 10b). We found almost exactly similar pattern between the high V_p/V_s and high attenuation anomalies in the northern Tarutung (profile A in Fig. 10a). Therefore the attenuation tomography validates and strengthens the previously proposed conceptual model
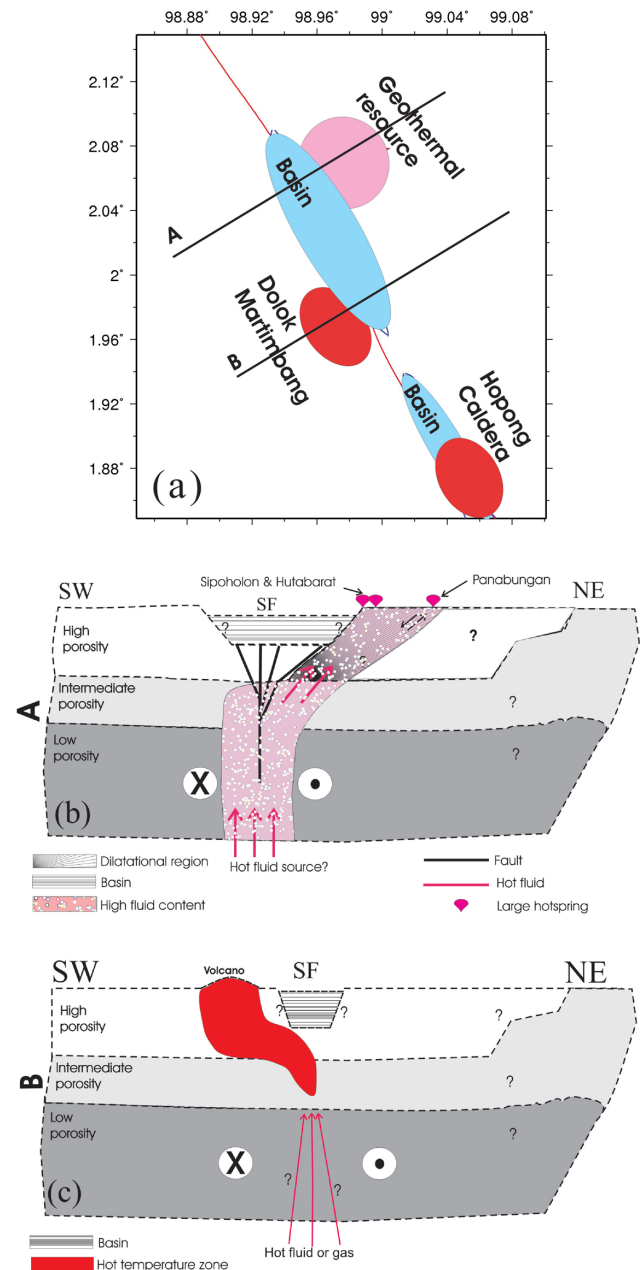
Figure 10. The new conceptual model derived from the attenuation tomography and complemented by the V_p/V_s tomography results (Muksin *et al.* 2013) describing four different clusters in Tarutung: (a) the map view of the new conceptual model of the Tarutung geothermal field, (b) the structure of the Tarutung geothermal area along the cross-section A and (c) the magmatic system of the Martimbang volcano indicated by the profile B. The hot fluid/gas is fed along the fault and transported to the southwest of the Sumatra Fault.

obtained from V_p and V_p/V_s tomography (Muksin *et al.* 2013) as shown in Fig. 10(b).

The red zones in the southwest of the Tarutung Basin and in Sarulla (Fig. 10a) represent the magmatic system in the region. Fig. 10(c) describes the magmatic system of the Martimbang volcano where the partial melt diapir is transported from the mantle along the fault zone. The conceptual model along the Sarulla Basin is similar to the one proposed in the V_p and V_p/V_s conceptual model (see fig. 19 in Muksin *et al.* 2013).

7 CONCLUSIONS

We have produced a well-resolved Q_p structure of the Tarutung geothermal area correlating with geothermal prospects and volcanism. Our study confirms that attenuation tomography is a powerful tool for the exploration of a geothermal site in a seismically active region. In Tarutung, the high attenuation zones are found along the Tarutung Basin associated with the basin sediment and in the northeast of Tarutung where the geothermal potentials are located. We image the magmatic system of the Martimbang volcano in the southwest of the Tarutung Basin showing the magma is fed along the fault and transported to the southwest of the Sumatra Fault. The low Q_p along the Sarulla graben is interpreted as the presence of the hot magma below the Hopong caldera. The geothermal system in Tarutung seems to be controlled mainly by the fault setting where the source of the hot fluid is originated from below the fault and transported to the northeast.

REFERENCES

Aki, K., 1967. Scaling law of seismic spectrum, *J. geophys. Res.,* **72**(4), 1217–1231.

Aki, K. & Chouet, B., 1975. Origin of coda waves: source, attenuation, and scattering effects, *J. geophys. Res.,* **80**(23), 3322–3342.

Aki, K. & Richards, P.G., 1980. *Quantitative Seismology,* Freeman & Co.

Anderson, D.L. & Given, J.W., 1982. Absorption band Q model for the Earth, *J. geophys. Res.,* **87**(B5), 3893–3904.

Artemieva, I.M., Billien, M., Lévêque, J.-J. & Mooney, W.D., 2004. Shear wave velocity, seismic attenuation, and thermal structure of the continental upper mantle, *J. geophys. Int.,* **157**, 607–628.

Atkinson, G.M., 2004. Empirical attenuation of ground-motion spectral amplitudes in southeastern Canada and the northeastern United States, *Bull. seism. Soc. Am.,* **94**(3), 1079–1095.

Bellier, O. & Sébrier, M., 1994. Relationship between tectonism and volcanism along the Great Sumatran Fault Zone deduced by spot image analyses, *Tectonophysics,* **233,** 215–231.

Bellier, O. & Sébrier, M., 1995. Is the slip rate variation on the Great Sumatran Fault accommodated by fore-arc stretching? *Geophys. Res. Lett.,* **22,** 1969–1972.

Boatwright, J., Fletcher, J.B. & Fumal, T.E., 1991. A general inversion scheme for source, site, and propagation characteristics using multiply recorded sets of moderate-sized earthquakes, *Bull. seism. Soc. Am.,* **81**(5), 1754–1782.

Bohm, M., Haberland, C. & Asch, G., 2013. Imaging fluid-related subduction processes beneath Central Java (Indonesia) using seismic attenuation tomography, *Tectonophysics,* **590,** 175–188.

Brune, J.N., 1970. Tectonic stress and the spectra of seismic shear waves from earthquakes, *J. geophys. Res.,* **75,** 4997–5009.

Brune, J.N., 1971. Correction, *J. geophys. Res.,* **76,** 5002.

Chung, J.-K., Chen, Y.-L. & Shin, T.-C., 2009. Spatial distribution of coda Q estimated from local earthquakes in Taiwan area, *Earth Planets Space,* **61**(9), 1077–1088.

De Lorenzo, S., Gasparini, P., Mongelli, F. & Zollo, A., 2001. Thermal state of the Campi Flegrei caldera inferred from seismic attenuation tomography, *J. Geodyn.,* **32,** 467–486.

De Siena, L., Del Pezzo, E. & Bianco, F., 2010. Seismic attenuation imaging of Campi Flegrei: evidence of gas reservoirs, hydrothermal basins, and feeding systems, *J. geophys. Res.,* **115,** B09312, doi:10.1029/2009JB006938.

Eberhart-Phillips, D., 1986. Three-dimensional velocity structure in Northern California Coast Ranges from inversion of local earthquake arrival times, *Bull. seism. Soc. Am.,* **76,** 1025–1052.

Eberhart-Phillips, D. & Chadwick, M., 2002. Three-dimensional attenuation model of the shallow Hikurangi subduction zone in the Raukumara Peninsula, New Zealand, *J. geophys. Res.: Solid Earth,* **107**(B2), ESE 3-1–ESE 3-15.

Eberhart-Phillips, D. & Michael, A.J., 1998. Seismotectonics of the Loma Prieta, California, region determined from three-dimensional *Vp*, *Vp/Vs*, and seismicity, *J. geophys. Res.,* **103,** 21 099–21 120.

Evans, J.R. & Zucca, J.J., 1988. Active high-resolution seismic tomography of compressional wave velocity and attenuation structure at Medicine Lake Volcano, Northern California Cascade Range, *J. geophys. Res.: Solid Earth,* **93,** 15 016–15 036.

Faul, U.H., Fitz Gerald, J.D. & Jackson, I., 2004. Shear wave attenuation and dispersion in melt-bearing olivine polycrystals: 2. Microstructural interpretation and seismological implications, *J. geophys. Res.: Solid Earth,* **109**(B6), B06202, doi:10.1029/2003JB002407.

Flanagan, M.P. & Wiens, D.A., 1990. Attenuation structure beneath the Lau back arc spreading center from teleseismic S phases, *Geophys. Res. Lett.,* **17**(12), 2117–2120.

Frankel, A. & Wennerberg, L., 1987. Energy-flux model of seismic coda: separation of scattering and intrinsic attenuation, *Bull. seism. Soc. Am.,* **77**(4), 1223–1251.

Gasparon, M., 2005. Quaternary volcanicity, in *Sumatra: Geology, Resources, and Tectonic Evolution,* pp. 120–130, eds Barber, A.J., Crow, M.J. & Milsom, J.S., Geological Society.

Gladwin, M.T. & Stacey, F., 1974. Anelastic degradation of acoustic pulses in rock, *Phys. Earth planet. Inter.,* **8**(4), 332–336.

Haberland, C. & Rietbrock, A., 2001. Attenuation tomography in the western central Andes: a detailed insight into the structure of a magmatic arc, *J. geophys. Res.,* **106,** 11 151–11 167.

Haberland, C., Rietbrock, A., Lange, D., Bataille, K. & Dahm, T., 2009. Structure of the seismogenic zone of the southcentral Chilean margin revealed by local earthquake traveltime tomography, *J. geophys. Res.: Solid Earth,* **114,** 1–17.

Hanks, T.C. & Wyss, M., 1972. The use of body-wave spectra in the determination of seismic-source parameters, *Bull. seism. Soc. Am.,* **62**(2), 561–589.

Hauksson, E. & Shearer, P.M., 2006. Attenuation models (Q_P and Q_S) in three dimensions of the southern California crust: inferred fluid saturation at seismogenic depths, *J. geophys. Res.: Solid Earth,* **111,** 1–21.

Hickman, R.G., Dobson, P.F., Gerven, M.V., Sagala, B.D. & Gunderson, R.P., 2004. Tectonic and stratigraphic evolution of the Sarulla graben geothermal area, North Sumatra, Indonesia, *J. Asian Earth Sci.,* **23,** 435–448.

Husen, S., Smith, R.B. & Waite, G.P., 2004. Evidence for gas and magmatic sources beneath the Yellowstone volcanic field from seismic tomographic imaging, *J. Volc. Geotherm. Res.,* **131,** 397–410.

Hwang, Y.K., Ritsema, J. & Goes, S., 2011. Global variation of body-wave attenuation in the upper mantle from teleseismic P wave and S wave spectra, *Geophys. Res. Lett.,* **38**(8), L06308, doi:10.1029/2011GL046812.

Julian, B.R., Ross, A., Foulger, G.R. & Evans, J.R., 1996. Three-dimensional seismic image of a geothermal reservoir: the Geysers, California, *Geophys. Res. Lett.,* **23,** 685–688.

Julian, B.R., Pitt, A.M. & Foulger, G.R., 1998. Seismic image of a CO2 reservoir beneath a seismically active volcano, *J. geophys. Int.,* **133,** F7–F10.

Karato, S.I., 2003. Mapping water content in the upper mantle, in *Inside the Subduction Factory, Geophys. Monogr. Ser.,* Vol. 138, pp. 135–152, ed. Eiler, J.M., AGU, Washington, DC.

Kissling, E., Ellsworth, W.L., Eberhart-Phillips, D. & Kradolfer, U., 1994. Initial reference models in local earthquake tomography, *J. geophys. Res.,* **99**(B10), 19 635–19 646.

Koulakov, I., Yudistira, T., Luehr, B.-G. & Wandono, 2009. *P, S* velocity and *Vp/Vs* ratio beneath the Toba caldera complex (Northern Sumatra) from local earthquake tomography, *J. geophys. Int.,* **177,** 1121–1139.

Lee, W.H.K. & Valdes, C.M., 1985. HYPO71PC: a personal computer version of the HYPO71 earthquake location program. Open-File Rep, U.S. Geol. Surv., 85–749.

Martínez-Arévalo, C., Patanè, D., Rietbrock, A. & Ibáñez, J.M., 2005. The intrusive process leading to the Mt. Etna 2001 flank eruption: constraints from 3-D attenuation tomography, *Geophys. Res. Lett.,* **32,** L21309, doi:10.1029/2005GL023736.

Mavko, G.M., 1980. Velocity and attenuation in partially molten rocks, *J. geophys. Res.: Solid Earth,* **85,** 5173–5189.

Mavko, G., Kjartansson, E. & Winkler, K., 1979. Seismic wave attenuation in rocks, *Rev. Geophys.,* **17,** 1155–1164.

McCaffrey, R., 2009. The tectonic framework of the Sumatran subduction zone, *Annu. Rev. Earth planet. Sci.,* **37,** 345–366.

Morozov, I.B., 2010. On the Causes of Frequency-Dependent Apparent Seismological Q, *Pure appl. Geophys.,* **167**(10), 1131–1146.

Muksin, U., Bauer, K. & Haberland, C., 2013. Seismic Vp and Vp/Vs structure of the geothermal area around Tarutung (North Sumatra, Indonesia) derived from local earthquake tomography, *J. Volc. Geotherm. Res.,* **260,** 27–42.

Muraoka, H., Takahashi, M., Sundhoro, H., Dwipa, S., Soeda, Y., Momita, M. & Shimada, K., 2010. Geothermal systems constrained by the Sumatran Fault and its pull-apart basins in Sumatra, western Indonesia, in *Proceedings of the World Geothermal Congress,* 2010 April 25–29, Bali, Indonesia.

Niasari, S., Munoz, G., Kholid, M., Suhanto, E. & Ritter, O., 2012. Magnetotelluric exploration of the Sipoholon geothermal field, Indonesia, *Geophys. Res. Abstr.,* **14,** doi:EGU2012-9405-1.

Nippress, S.E.J., Rietbrock, A. & Heath, A.E., 2010. Optimized automatic pickers: application to the ANCORP data set. *J. geophys. Int.,* **181,** 911–925.

Park, J., Lindberg, C.R. & Vernon, F.L. III, 1987. Multitaper spectral analysis of high-frequency seismograms, *J. geophys. Res.,* **92,** 12 675–12 684.

Pesicek, J.D., Thurber, C.H., Widiyantoro, S., Zhang, H., DeShon, H.R. & Engdahl, E.R., 2010. Sharpening the tomographic image of the subducting slab below Sumatra, the Andaman Islands and Burma, *J. geophys. Int.,* **182**(1), 433–453.

Priyono, A., Suantika, G., Widiyantoro, S. & Nugraha, A.D., 2011. Three-dimensional seismic attenuation structure of Mt. Guntur, West Java, Indonesia, *Int. J. Tomogr. Statist.,* **17,** 17–28.

Quan, Y. & Harris, J.M., 1997. Seismic attenuation tomography using the frequency shift method, *Geophysics,* **62**(3), 895–905.

Rietbrock, A., 2001. P wave attenuation structure in the fault area of the 1995 Kobe earthquake, *J. geophys. Res.,* **106,** 4141–4154.

Sanders, C.O., 1993. Local earthquake tomography: attenuation—theory and results, in *Seismic Tomography: Theory and Practice,* pp. 676–694, eds Iyer, H. & Hirahara, K., Chapmann and Hall.

Sato, H., Sacks, I.S., Murase, T., Muncill, G. & Fukuyama, H., 1989. *Qp*-melting temperature relation in peridotite at high pressure and temperature: attenuation mechanism and implications for the mechanical properties of the upper mantle, *J. geophys. Res.: Solid Earth,* **94,** 10 647–10 661.

Scherbaum, F., 1990. Combined inversion for the three-dimensional Q structure and source parameters using microearthquake spectra, *J. Geophys. Res.,* **95,** 12 423–12 438.

Schurr, B., Asch, G., Rietbrock, A., Trumbull, R. & Haberland, C., 2003. Complex patterns of fluid and melt transport in the central Andean subduction zone revealed by attenuation tomography, *Earth planet. Sci. Lett.,* **215**(1), 105–119.

Sieh, K. & Natawidjaja, D., 2000. Neotectonics of the Sumatran fault, Indonesia, *J. geophys. Res.,* **105**(28), 295–326.

Stankiewicz, J., Ryberg, T., Haberland, C., Fauzi & Natawidjaja, D., 2010. Lake Toba volcano magma chamber imaged by ambient seismic noise tomography, *Geophys. Res. Lett.,* **37,** L17306, doi:10.1029/2010GL044211.

Takanami, T., Selwyn Sacks, I. & Hasegawa, A., 2000. Attenuation structure beneath the volcanic front in northeastern Japan from broad-band seismograms, *Phys. Earth planet. Inter.,* **121,** 339–357.

Thurber, C., 1983. Earthquake locations and three-dimensional crustal structure in the Coyote Lake Area, Central California, *J. geophys. Res.,* **88,** 8226–8236.

Toomey, D.R. & Foulger, G.R., 1989. Tomographic inversion of local earthquake data from the Hengill-Grensdalur central volcano complex, Iceland, *J. geophys. Res.,* **94,** 17 497–17 510.

Walsh, J., 1995. Seismic attenuation in partially saturated rock, *J. geophy. Res.,* **100,** 15 407–15 424.

Wang, Z. & Nur, A., 1990. Wave velocities in hydrocarbon-saturated rocks; experimental results, *Geophysics,* **55,** 723–733.

Wu, H. & Lees, J.M., 1996. Attenuation structure of Coso geothermal area, California, from wave pulse widths, *Bull. seism. Soc. Am.,* **86,** 1574–1590.

Yang, X., Lay, T., Xie, X.-B. & Thorne, M.S., 2007. Geometric spreading of Pn and Sn in a spherical Earth model, *Bull. seism. Soc. Am.,* **97**(6), 2053–2065.

Zucca, J.J. & Evans, J.R., 1992. Active high-resolution compressional wave attenuation tomography at Newberry Volcano, Central Cascade Range, *J. geophys. Res.: Solid Earth,* **97,** 11 047–11 055.

Zucca, J.J., Hutchings, L.J. & Kasameyer, P.W., 1994. Seismic velocity and attenuation structure of the Geysers geothermal field, California, *Geothermics,* **23,** 111–126.